analytical chemistry

pubs.acs.org/ac Article

Machine Learning-Assisted Nanozyme–Porphyrin Dual-Channel Sensor Array for Glycosaminoglycan Pattern Recognition

Sijie Li,[#] Qing Cheng,[#] Qi Sun, Chunfei Bao, Guangyu Bu, Shuaishuai Zhu, Yubin Ding,* Hui Wei,* and Xiaoyu Wang*

Cite This: https://doi.org/10.1021/acs.analchem.6c03852 Read Online

ACCESS | Metrics & More | Article Recommendations | Supporting Information

ABSTRACT: Selective discrimination of glycosaminoglycans (GAGs) is crucial for drug safety and quality control but remains challenging because GAGs share similar disaccharide repeating units and overlapping polyanionic features. Nanozyme-based sensor arrays offer a cross-reactive fingerprinting strategy, yet many require multiple nanozymes with single readouts and correlated responses, increasing operational complexity and limiting pattern separability. Herein, we constructed a dual-channel sensor array by assembling two cationic near-infrared (NIR) porphyrins with a multifunctional Pt–Ni/rGO nanozyme that integrated efficient fluorescence quenching and oxidase-like catalysis. Upon GAG binding, each sensing element generated dual outputs, including NIR fluorescence response driven by competitive association between anionic GAGs and cationic porphyrins, and characteristic UV–vis absorption changes arising from Pt–Ni/rGO-catalyzed TMB oxidation to TMBox followed by TMBox–GAG assembly. Machine learning analysis of the four cross-reactive signals generated by the two sensing elements enabled 100% accurate discrimination of hyaluronic acid, heparin, dextran sulfate, and chondroitin sulfate in PBS over 25–500 μg/mL. Its practical utility was further demonstrated by identifying trace GAG contaminants in Hep down to 1%, classifying unknown samples, and discriminating GAGs in serum. This work expands the analytical utility of multifunctional nanozymes and provides a simple strategy for fingerprint-based GAG analysis with enhanced signal dimensionality and separability.

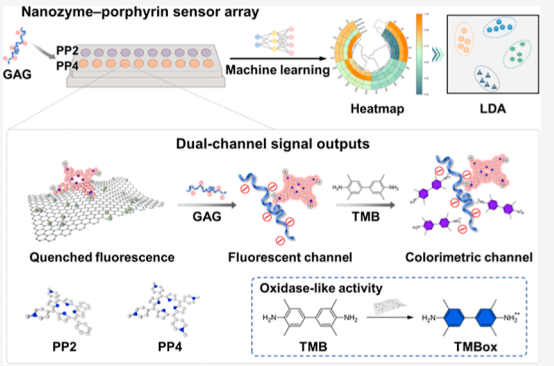

INTRODUCTION

Glycosaminoglycans (GAGs) are naturally occurring, unbranched linear polysaccharides that regulate diverse biological processes and thus are of considerable clinical significance.[1−3] For example, heparin (Hep) is widely used as an anticoagulant in surgery and hemodialysis, whereas chondroitin sulfate (Chs) is commonly administered for osteoarthritis.[4,5] Selective discrimination of GAGs is critical for drug safety and quality control, particularly for Hep, which is typically isolated from animal tissues and may be contaminated or adulterated with structurally related polyanions such as hyaluronic acid (HA), dextran sulfate (DSS), and Chs.[4,6,7] The contamination of Hep products by related polyanionic polysaccharides caused a serious safety event in 2008, highlighting the need for reliable identification of Hep impurities during pharmaceutical quality control.[8] However, accurate differentiation remains challenging because many GAGs share closely related disaccharide repeating units and overlapping polyanionic features.[2,3,7] Although established techniques such as nuclear magnetic resonance (NMR), high-performance liquid chromatography (HPLC), and liquid chromatography–tandem mass spectrometry (LC–MS/MS) enable reliable characterization, they generally require costly instrumentation and expert data interpretation, limiting their utility for routine and rapid screening.[6,9,10] Fluorophore-based probes, including BODIPY, pyrene, porphyrins, rhodamine, and aggregation-induced emission luminogens, have therefore been developed for GAG sensing owing to their operational simplicity and high sensitivity.[11−17] Nevertheless, most fluorescent GAG sensors rely predominantly on multivalent electrostatic interactions between cationic dyes and anionic GAG chains, making highly selective "lock-and-key" recognition intrinsically difficult for this class of structurally similar polyanions.

Compared with highly specific "lock-and-key" recognition, cross-reactive sensor arrays, inspired by mammalian gustatory and olfactory systems, distinguish structurally similar analytes by converting differential nonspecific interactions into fingerprint-like response patterns.[18−22] In this regard, nanomaterials with enzyme-like activities (i.e., nanozymes) offer an attractive

Received: June 4, 2026
Revised: August 23, 2026
Accepted: August 27, 2026

Scheme 1. Schematic Illustration of Pt−Ni/rGO−Porphyrin-Based Single-Nanozyme Dual-Channel Sensor Array for Pattern Recognition of GAGs

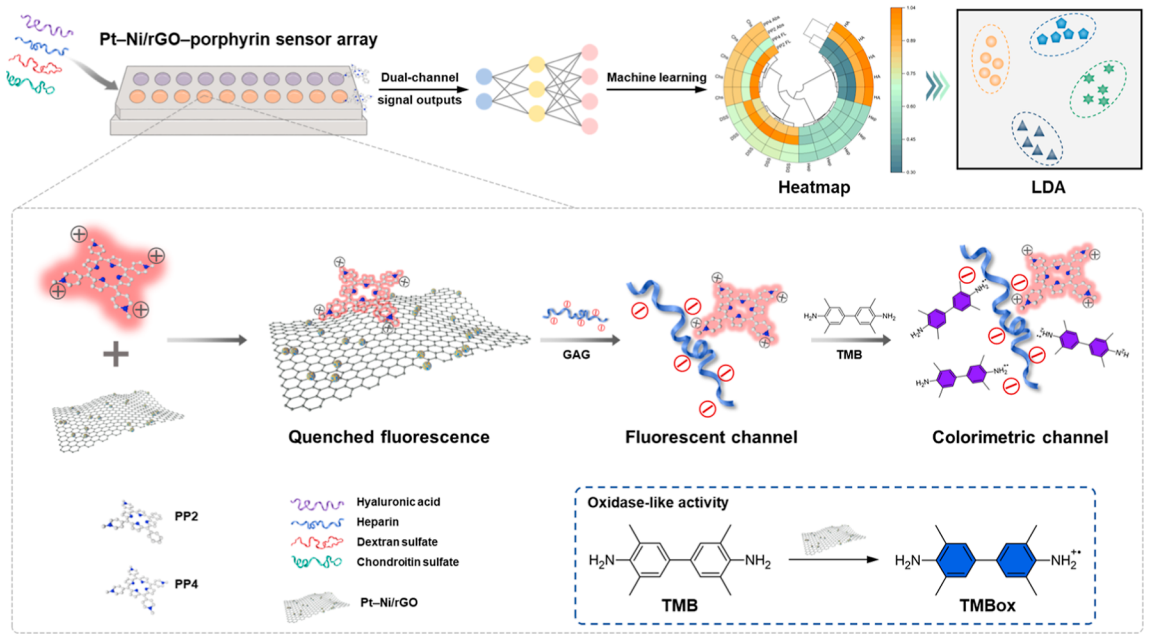

platform for array construction because they combine large surface areas, tunable catalytic activities, robust stability, and multifunctionality beyond catalysis.[23−29] Accordingly, nanozyme-based arrays have been increasingly explored for fingerprint-style identification.[30−40] For example, oxidase-like manganese/cerium-codoped carbon dot−loaded MIL-53(Fe) nanozymes have been used to generate multicolor outputs for discriminating structurally analogous antioxidants.[41] Similarly, cerium-based metal−organic framework with multienzyme-mimicking activities have enabled multichannel discrimination of perfluoroalkyl substances by converting analyte-dependent modulation of catalytic pathways into distinct readouts.[42] Despite these advances, many nanozyme-based arrays still require multiple sensing elements that each provide only a single output, increasing material consumption and operational complexity.[30,31,35] In addition, array elements that share similar recognition and signal-transduction mechanisms often produce correlated responses, which can reduce cross-reactivity and pattern separability.[31,43−45] For example, in an oxidase-like Mn-based metal−organic framework nanozyme array for antioxidant discrimination, all sensing elements employed the same inhibition-based signal transduction mechanism. Consequently, antioxidants with different reducing abilities produced similar response trends across the array, resulting in correlated outputs. Therefore, integrating distinct signal-generation pathways into sensor arrays is highly desirable for improving pattern recognition performance.[44]

Beyond catalytic activity, nanozymes also inherit the intrinsic physicochemical properties of nanomaterials, including optical, magnetic, and surface plasmon resonance features.[46−49] Integrating enzyme-like catalysis with these properties enables multifunctional nanozymes to couple target interaction, signal transduction, and amplification within a single material system.[28] For example, nanoceria can adsorb fluorophore-labeled single-stranded DNA and quench its emission; upon exposure to H_2O_2, surface changes weaken DNA binding and restore fluorescence.[46] Plasmonic nanozyme hybrids can also combine catalytic conversion with electromagnetic enhancement for ultrasensitive surface-enhanced Raman scattering detection, extending nanozyme readouts beyond conventional colorimetry.[49−51] These examples indicate that rational use of nanozyme multifunctionality can allow a single nanozyme-based sensing element to generate multiple, mechanistically distinct outputs, increasing signal dimensionality while simplifying array construction.[31,52,53]

Herein, we reported a dual-channel sensor array based on a multifunctional Pt−Ni/rGO nanozyme that integrated efficient fluorescence quenching with oxidase-like catalysis. Two cationic near-infrared (NIR) porphyrins, PP2 and PP4, were assembled onto Pt−Ni/rGO to form two nanozyme−porphyrin composites as sensing elements (Scheme 1). Upon exposure to GAGs, each sensing element produced dual outputs. Competitive association between anionic GAGs and cationic porphyrins weakened the nanozyme−porphyrin interaction, resulting in NIR fluorescence response. Meanwhile, Pt−Ni/rGO catalyzed the oxidation of 3,3′,5,5′-tetramethylbenzidine (TMB) to oxidized TMB (TMBox), whose subsequent assembly with GAGs induced characteristic UV−vis absorption changes (Scheme 1). The two sensing elements therefore provided four cross-reactive signals for GAG discrimination. Through machine learning-assisted pattern recognition, the array accurately discriminated representative GAGs, including HA, Hep, DSS, and Chs, in PBS over 25−500 μg/mL with 100% classification accuracy. It also identified trace GAG contaminants in Hep down to 1% and demonstrated practical utility through unknown-sample identification and GAG discrimination in serum. Overall, this work expands the analytical utility of multifunctional nanozymes and provides a simple, robust strategy for fingerprint-based GAG analysis with enhanced signal dimensionality and separability.

https://doi.org/10.1021/acs.analchem.6c03852
Anal. Chem. XXXX, XXX, XXX−XXX

EXPERIMENTAL SECTION

Chemicals and Materials

3,3′,5,5′-tetramethylbenzidine (TMB), sodium hyaluronate (HA), chondroitin sulfate (Chs), benzyl alcohol, low-molecular-weight heparin (M_w 2000−3000) and benzoic acid were purchased from Aladdin Chemical Co., Ltd. Heparin sodium salt (Hep) were obtained from TCI Development Co., Ltd. Dextran sulfate sodium (DSS) was purchased from MP Biomedicals, USA. Polyvinylpyrrolidone (PVP, M_w 55,000) were obtained from Sigma-Aldrich. Fetal bovine serum was obtained from Zhejiang Tianhang Biotechnology Co., Ltd. Platinum(II) acetylacetonate (Pt(acac)2) and nickel(II) acetylacetonate (Ni(acac)2) were obtained from J&K Scientific Co., Ltd. Graphene oxide (GO) was purchased from Jiangsu Xianfeng Nanomaterials Technology Co. Ltd. Acetone and nitric acid (HNO_3) were purchased from Sinopharm Chemical Reagent Co., Ltd. Hydrochloric acid (HCl) was purchased from Nanjing Chemical Reagent Co., Ltd. All aqueous solutions used in the experiments were prepared with deionized water (18.2 MΩ·cm, Millipore).

Instrumentation

Transmission electron microscopy (TEM) imaging was performed on a Tecnai 12 (Philips company, Holland) transmission electron microscope at an acceleration voltage of 120 kV. High-resolution transmission electron microscopy (HRTEM) was performed on a JEM-2800 (JEOL, Japan) transmission electron microscope at an acceleration voltage of 200 kV. High-angle annular dark-field scanning TEM (HAADF-STEM), and the corresponding energy-dispersive spectroscopy (EDS) elemental mappings were performed on an FEI Tecnai G2 F30 S-Twin TEM equipped with an acceleration voltage of 300 kV and an EDS detector, respectively. Scanning electron microscopy (SEM) imaging was performed on an FEI Inspect F50. Powder X-ray diffraction (XRD) patterns were measured by a Bruker D8 advance diffractometer at 5°/min using a Cu Kα radiation. X-ray photoelectron spectra (XPS) were obtained by using a Thermo Scientific Nexsa G2 surface analysis system. Inductively coupled plasma-optical emission spectroscopy (ICP-OES) measurements were conducted using a Thermo Scientific iCAP PRO spectrometer. ^{1}H NMR spectra were obtained using a Bruker Advance 500 MHz spectrometer with tetramethylsilane as the internal standard. High resolution mass spectrum (HRMS) was measured on an AB SCIEX TripleTOF 5600$^+$ mass spectrometer. Absorption spectra were collected using a UV-2700 spectrophotometer (Shimadzu, Japan). Fluorescence spectra were recorded using an FS5 fluorescence spectrometer (Edinburgh Instruments, UK). The fluorescence at 670 nm and absorption at 370 nm of the 96-well plate was recorded by a BioTek Cytation 3 microplate reader (Agilent, USA).

Synthesis of PP2 and PP4

Two cationic NIR porphyrins (PP2 and PP4) were synthesized following our previously reported procedure.[13]

Synthesis of Pt−Ni/rGO

Pt−Ni/rGO nanozyme was synthesized as follows. Briefly, Pt(acac)2 (60.63 mg, 0.15 mmol), Ni(acac)2 (39.60 mg, 0.15 mmol), benzoic acid (300 mg), PVP (80 mg), and GO (64 mg) were dispersed in benzyl alcohol (30 mL) under vigorous magnetic stirring. The mixture was sonicated for 30 min to obtain a homogeneous dispersion, transferred to a Teflon-lined autoclave, and heated at 180 °C for 12 h. After cooling to room temperature, the product was collected by centrifugation (11,000 rpm, 5 min) and washed 3× with ethanol. The purified Pt−Ni/rGO was then dried under vacuum at 40 °C overnight.

Pt−Ni/rGO composites with different Pt−Ni to GO mass ratios were synthesized using the same procedure, except that the amount of GO was varied. Specifically, GO amounts of 32, 128, and 192 mg were used to obtain Pt−Ni/rGO-2, Pt−Ni/rGO-8, and Pt−Ni/rGO-12, respectively. As a control, Pt−Ni nanoparticles (NPs) were synthesized under identical conditions, except that GO was not added to the reaction mixture.

Fluorescence Spectrum Measurements

Stock solutions of PP2 and PP4 (10 mM) were prepared in DMF and diluted with PBS (pH 6.8) to the desired concentrations immediately before use. For fluorescence quenching measurements, PP2 or PP4 (final concentration, 4 μM) was incubated with Pt−Ni/rGO in PBS (pH 6.8) for 20 min, with the Pt−Ni/rGO concentration varied from 0 to 100 μg/mL. Emission spectra were collected under excitation at 423 nm. For fluorescence response measurements, PP2 or PP4 (4 μM) was mixed with Pt−Ni/rGO (60 μg/mL) and the indicated GAG in PBS (pH 6.8), incubated for 20 min, and then subjected to fluorescence measurement.

Oxidase-like Activity Measurements

The oxidase-like activities of Pt−Ni NPs and Pt−Ni/rGO were evaluated by steady-state kinetics assays using TMB as the substrate.[54] Briefly, the assays were performed at 25 °C in 96-well microplates using acetate buffer (0.2 M, pH 4.5) as the reaction medium. Pt−Ni NPs (5 μg/mL) or Pt−Ni/rGO (16.67 μg/mL, containing 5 μg/mL of Pt−Ni) was mixed with varying concentrations of TMB. The absorbance at 652 nm was immediately monitored using a microplate reader, and the resulting absorbance−time curves were used to calculate the initial reaction velocity (v). The kinetic parameters, including the Michaelis−Menten constant (K_m) and maximum reaction velocity (v_{max}), were obtained by fitting the data to the Michaelis−Menten equation

$$v = \frac{v_{max}[S]}{K_m + [S]} \quad (1)$$

where v represents the initial reaction velocity and $[S]$ is the substrate concentration. K_m and v_{max} were calculated from the corresponding double-reciprocal plots.

UV−Vis Absorption Measurements

PP2 or PP4 (final concentration, 4 μM), Pt−Ni/rGO (60 μg/mL), and the indicated GAG were mixed in PBS (pH 6.8) and incubated at room temperature for 20 min. TMB was then added to a final concentration of 200 μM, followed by further incubation for 10 min at room temperature. The UV−vis absorption spectra were subsequently recorded using a UV−vis spectrophotometer.

GAG Discrimination Assay

Discrimination experiments were performed in 96-well plates, and the responses were recorded as data matrices. For each Pt−Ni/rGO−porphyrin composite, namely Pt−Ni/rGO−PP2 and Pt−Ni/rGO−PP4, a 4 × 5 block of wells was assigned, with each GAG measured in five replicates. In each well, PP2 or PP4, Pt−Ni/rGO, and the indicated GAG were mixed in PBS (pH 6.8) to a final volume of 200 μL, giving final concentrations of 4 μM porphyrin and 60 μg/mL Pt−Ni/rGO. After incubation for 20 min, the fluorescence intensity at 670 nm was recorded using a microplate reader upon excitation at 423 nm. TMB was then added to each well to a final concentration of 200 μM, mixed thoroughly, and incubated for 10 min before measuring the absorbance at 370 nm. The fluorescence and UV−vis absorption outputs from the two composites were combined to construct a training matrix with five replicates per GAG, which was subsequently analyzed by linear discriminant analysis (LDA) for pattern recognition.

Discrimination Experiments in Serum Media

To demonstrate the practical applicability of the sensor array to real samples, discrimination experiments were performed in fetal bovine serum (FBS). The assay followed the same protocol as in PBS, except that the concentrations of Pt−Ni/rGO and TMB were increased to 100 μg/mL and 400 μM, respectively, and the incubation time after TMB addition was extended to 20 min before measuring the absorbance at 370 nm. GAG stock solutions were prepared in PBS containing 2% or 5% (v/v) FBS.

https://doi.org/10.1021/acs.analchem.6c03852
Anal. Chem. XXXX, XXX, XXX−XXX

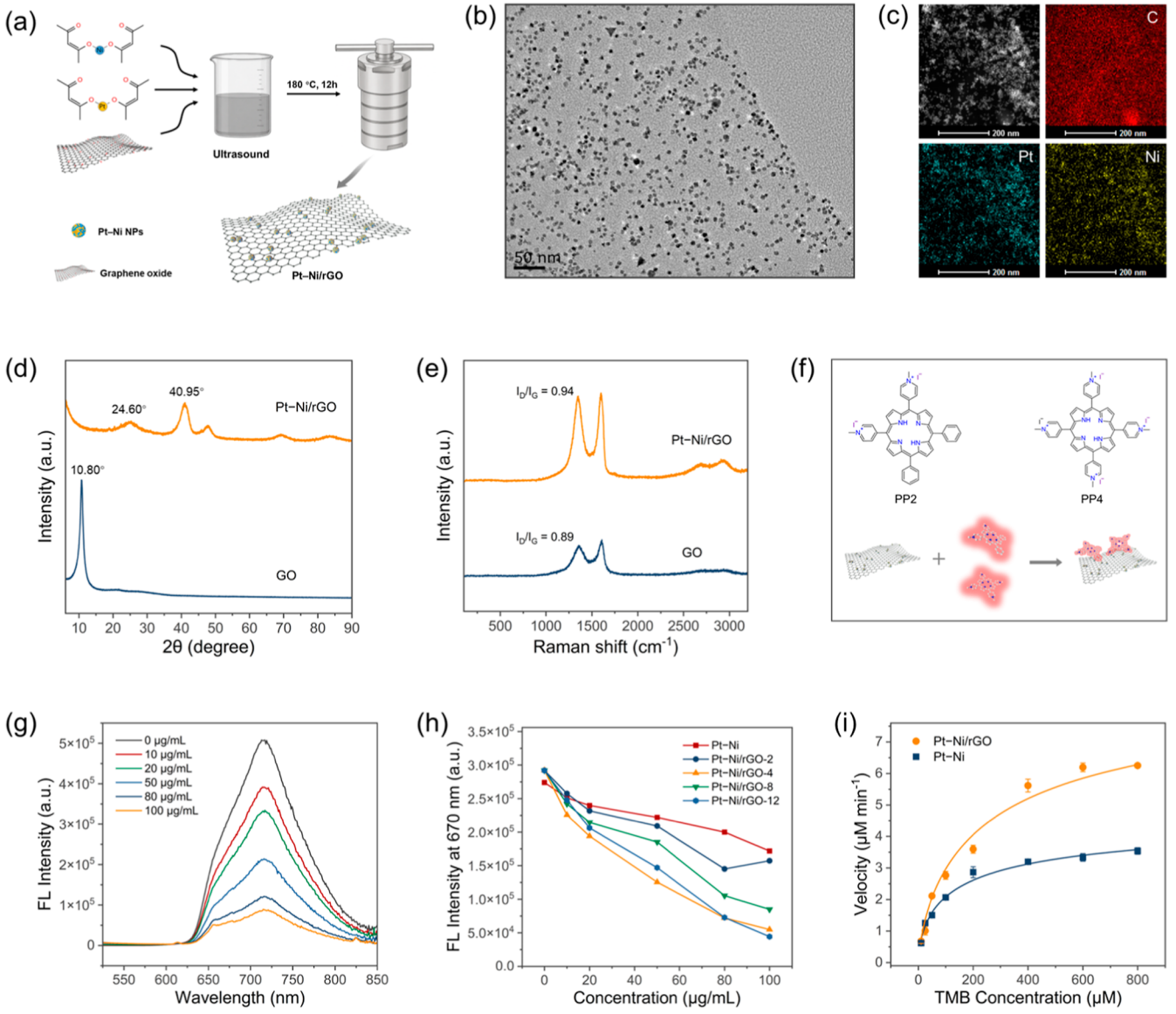

Figure 1. (a) Schematic illustration of synthesis for Pt–Ni/rGO. (b) TEM image of Pt–Ni/rGO. (c) HAADF-STEM image and corresponding EDS elemental mapping of Pt–Ni/rGO. (d) Powder X-ray diffraction patterns and (e) Raman spectra of GO and Pt–Ni/rGO. (f) Schematic illustration of fluorescence quenching of porphyrins by Pt–Ni/rGO. (g) Fluorescence titration profiles of PP4 (4 μM) upon addition of Pt–Ni/rGO at increasing concentrations (0–100 μg/mL) in PBS (10 mM, pH 6.8). (h) Fluorescence emission intensity of PP4 at 670 nm as a function of added nanozyme concentration. (i) Plots of initial reaction velocity versus TMB concentration for Pt–Ni (5 μg/mL) and Pt–Ni/rGO (16.67 μg/mL, containing 5 μg/mL Pt–Ni) in acetate buffer (0.2 M, pH 4.5). Error bars represent standard deviation of three independent measurements.

RESULTS AND DISCUSSION

Synthesis and Characterization of Pt–Ni/rGO

Previous studies have shown that Pt–Ni NPs can exhibit enhanced oxidase-like activity relative to Pt.[55] Guided by this rationale, Pt–Ni/rGO (reduced graphene oxide, rGO) was synthesized via a one-pot hydrothermal route by in situ growth of Pt–Ni NPs on graphene oxide (GO) (Figure 1a; see the Experimental Section for details), using a GO mass 4× that of Pt–Ni obtained from the GO-free synthesis. TEM images showed that Pt–Ni NPs were uniformly distributed on rGO sheets (Figures 1b and S1), whereas Pt–Ni NPs synthesized without GO showed severe aggregation (Figure S2), highlighting the dispersion-stabilizing role of rGO. HAADF-STEM imaging and EDS mapping further confirmed the homogeneous distribution of C, Pt, and Ni in the composite (Figure 1c). HRTEM revealed a lattice spacing of 0.219 nm, slightly smaller than that of fcc Pt(111) (0.225 nm), consistent with lattice contraction caused by Ni incorporation (Figures S1 and S2). XRD provided evidence for both GO reduction and Pt–Ni formation. The GO (001) diffraction peak at $2\theta \approx 10.80°$ was markedly weakened after hydrothermal treatment, while a broad peak near $2\theta \approx 24.60°$ emerged, which can be assigned to the rGO (002) reflection and indicated partial deoxygenation and restacking of GO (Figure 1d). In addition, an fcc diffraction peak centered at $2\theta \approx 40.95°$ was observed, consistent with the formation of Pt–Ni NPs.[55] Raman spectra showed pronounced D (1349 cm^{-1}) and G (1602 cm^{-1}) bands for Pt–Ni/rGO (Figure 1e). The overall enhancement may arise from the surface-enhanced Raman scattering effect of the bimetallic NPs, while the increased I_D/I_G ratio suggests defect generation accompanying GO reduction.[56] XPS further

https://doi.org/10.1021/acs.analchem.6c03852
Anal. Chem. XXXX, XXX, XXX–XXX

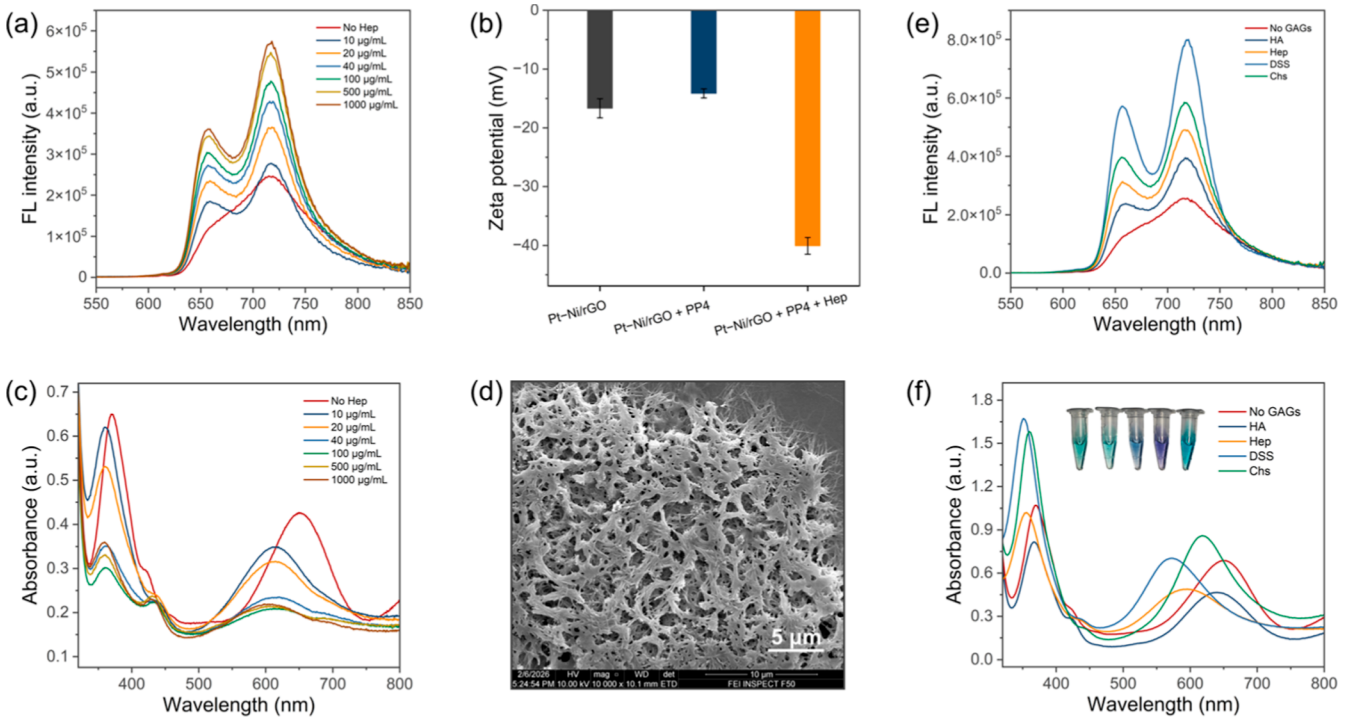

Figure 2. (a) Fluorescence response of Pt−Ni/rGO−PP4 nanocomposite toward increasing concentrations of Hep (0−1000 μg/mL) in PBS (10 mM, pH 6.8). (b) Zeta potentials of Pt−Ni/rGO and Pt−Ni/rGO−PP4 nanocomposite measured in the absence and presence of Hep (100 μg/mL). Error bars represent standard deviation of three independent measurements. (c) UV−vis absorption spectra of Pt−Ni/rGO−PP4−TMB system in the presence of Hep (0−1000 μg/mL). (d) SEM images of reaction products obtained after incubating PP4 (4 μM) and Hep (200 μg/mL) with Pt−Ni/rGO (60 μg/mL) for 20 min, followed by addition of TMB (200 μM) and further incubation for 10 min. (e) Fluorescence response of Pt−Ni/rGO−PP4 nanocomposite toward various GAGs (100 μg/mL). (f) UV−vis absorption spectra of Pt−Ni/rGO−PP4−TMB system in the presence of various GAGs (200 μg/mL). Inset: corresponding photographs showing visual color changes from left to right: no GAGs, HA, Hep, DSS, and Chs.

supported these results, showing decreased O 1s intensity together with Pt 4f and Ni 2p signals (Figure S3). Collectively, these characterizations confirmed the in situ growth and effective immobilization of Pt−Ni NPs on rGO, affording a well-dispersed Pt−Ni/rGO composite for subsequent bioanalysis.

In addition to the above Pt−Ni/rGO (denoted Pt−Ni/rGO-4), composites with GO loadings of 2×, 8×, and 12× were synthesized and labeled as Pt−Ni/rGO-2, Pt−Ni/rGO-8, and Pt−Ni/rGO-12, respectively (Figures S4−S6).

Fluorescent-Quenching Property and Oxidase-like Activity

Two cationic NIR porphyrins, PP2 and PP4, were synthesized following our previously reported procedure[13] and confirmed by ^{1}H NMR and mass spectrometry (Figures S7−S10). Their different numbers and positions of 4-*N*-methylpyridyl groups may tune their binding affinities toward GAGs, potentially facilitating differential fluorescence responses for array-based discrimination. We first examined the fluorescence-quenching ability of bare Pt−Ni NPs toward the two porphyrins. As shown in Figure S11, Pt−Ni NPs partially quenched PP2 but showed only weak quenching toward PP4, indicating that Pt−Ni NPs alone were insufficient to provide an efficient fluorescence-responsive interface. Considering that GO can quench cationic porphyrins through electrostatic adsorption, $\pi-\pi$ interactions, and assembly-induced effects,[13] we next evaluated the Pt−Ni/rGO composites (Figures 1f,g and S12−S15). Quantitative analysis showed that the quenching efficiency generally increased with increasing GO content (Figures 1h and S16). Pt−Ni/rGO-4, Pt−Ni/rGO-8, and Pt−Ni/rGO-12 exhibited comparable quenching efficiencies, whereas Pt−Ni/rGO-2 showed weaker quenching, likely because the high surface density and partial aggregation of Pt−Ni NPs limited effective porphyrin and rGO interactions (Figures 1h, S4−S6, S12 and S16). Although Pt−Ni/rGO-8 and Pt−Ni/rGO-12 showed quenching performance similar to that of Pt−Ni/rGO-4, their lower Pt−Ni loading would be less favorable for producing strong catalytic colorimetric signals (Figure S17). Pure GO showed the highest quenching efficiency toward both porphyrins at 100 μg/mL (Figure S18), which can be ascribed to abundant oxygen-containing groups that facilitate porphyrin adsorption and $\pi-\pi$ stacking.[13] However, GO exhibited negligible oxidase-like activity (Figure S19a). Therefore, considering both fluorescence quenching and catalytic output, Pt−Ni/rGO-4 was selected for subsequent experiments and is hereafter referred to as Pt−Ni/rGO.

The oxidase-like activity of Pt−Ni/rGO was evaluated using TMB as the chromogenic substrate (Figure S19). At an equivalent Pt−Ni content (30 μg/mL, calculated from ICP results; Table S1), both Pt−Ni NPs and Pt−Ni/rGO efficiently catalyzed TMB oxidation to blue oxidized TMB (TMBox). Notably, Pt−Ni/rGO produced a stronger absorbance at 652 nm than bare Pt−Ni NPs, suggesting that rGO-supported dispersion improved catalytic efficiency by exposing more accessible active sites and facilitating substrate contact (Figure S19). Steady-state kinetic assays further quantified this enhancement. Michaelis−Menten curves were obtained by plotting the initial reaction velocity against TMB

https://doi.org/10.1021/acs.analchem.6c03852
Anal. Chem. XXXX, XXX, XXX−XXX

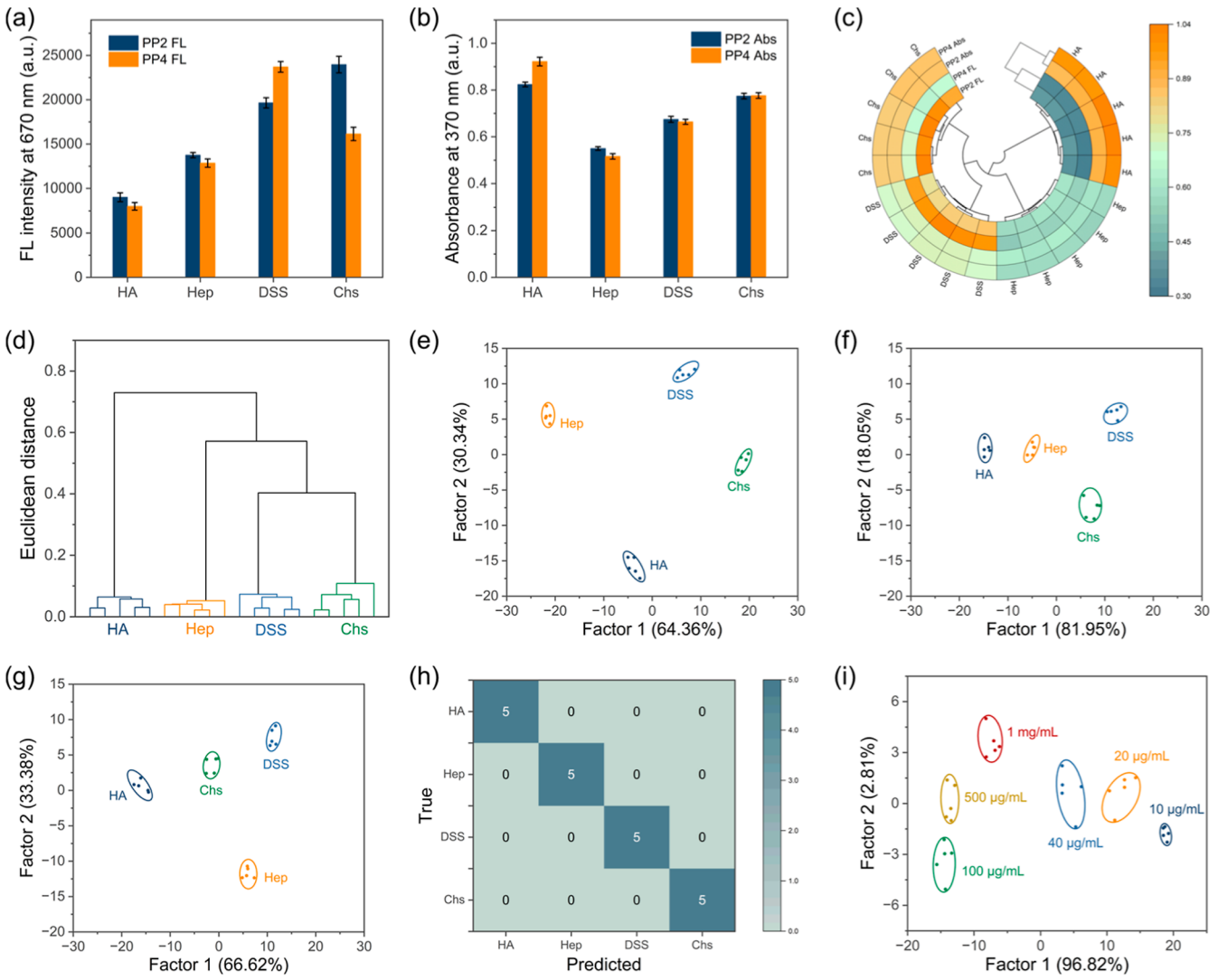

Figure 3. Fluorescence (a) and colorimetric (b) response patterns of Pt−Ni/rGO−PP2 and Pt−Ni/rGO−PP4 sensor array toward GAGs (100 μg/mL). Error bars represent standard deviation of five independent measurements. (c) Hierarchical clustering heatmap of normalized response signals. (d) HCA dendrogram for discrimination of GAGs (100 μg/mL). LDA canonical score plot for the first two factors obtained from (e) fluorescence and colorimetric responses of Pt−Ni/rGO−PP2 and Pt−Ni/rGO−PP4 sensor array toward GAGs (100 μg/mL), (f) fluorescence responses only of the same sensor array, and (g) fluorescence and colorimetric responses of Pt−Ni/rGO−PP4 single sensor toward GAGs (100 μg/mL). (h) Confusion matrix plot of LDA classifier for blind test in PBS (10 mM, pH 6.8). (i) LDA canonical score plot for the first two factors obtained from fluorescence and colorimetric responses of Pt−Ni/rGO−PP2 and Pt−Ni/rGO−PP4 sensor array toward Hep at different concentrations (10−1000 μg/mL).

concentration (Figure 1i), and kinetic parameters, including K_m and v_{max}, were derived from Lineweaver−Burk plots (Figure S20 and Table S2). Consistent with the activity assay, Pt−Ni/rGO exhibited a higher v_{max} toward TMB than bare Pt−Ni NPs under equivalent Pt−Ni content, with values of 7.23 and 3.86 μM/min, respectively (Table S2). These results indicated that Pt−Ni/rGO integrated efficient fluorescence-quenching capability with strong oxidase-like catalysis, providing a suitable dual-channel fluorescence−colorimetric platform for subsequent GAG discrimination.

Sensing Mechanism for GAGs Detection

To elucidate the response mechanism of GAGs toward the Pt−Ni/rGO−porphyrin composites, Hep was first used as a model analyte to evaluate both the fluorescence and colorimetric outputs of Pt−Ni/rGO−PP4. As shown in Figure 2a, the quenched fluorescence of PP4 was progressively restored with increasing Hep concentration, giving a clear concentration-dependent response. Zeta-potential measurements supported the electrostatic assembly between negatively charged Pt−Ni/rGO and cationic PP4, leading to formation of the Pt−Ni/rGO−PP4 composite (Figure 2b). Upon addition of highly anionic Hep, surface-bound PP4 was partially displaced from Pt−Ni/rGO through competitive PP4−Hep association, resulting in fluorescence response. Meanwhile, partial adsorption of Hep onto the Pt−Ni/rGO−PP4 assembly further shifted the surface potential to more negative values (Figure 2a,b). The colorimetric response was then investigated based on the oxidase-like activity of Pt−Ni/rGO, which catalyzes the oxidation of colorless TMB to blue oxidized TMB (TMBox). After TMB was introduced into the Pt−Ni/rGO−PP4 system, the generated positively charged TMBox assembled with Hep through electrostatic interactions,[57] producing new absorption features and inducing blue shifts of the original TMBox absorption peaks at approximately 370

https://doi.org/10.1021/acs.analchem.6c03852
Anal. Chem. XXXX, XXX, XXX−XXX

and 650 nm (Figure 2c). With increasing Hep concentration, the absorption intensity in the 300−400 nm region gradually changed, indicating progressive formation of Hep−TMBox assemblies (Figure 2c). Zeta-potential measurements confirmed Hep−TMBox assembly, with the Hep−TMBox complex showing a distinct zeta potential of −19.67 mV compared with positive TMBox and highly negative Hep (Figure S21). SEM imaging further supported this assembly process, revealing distinct fibrous structures in the presence of Hep, whereas the control without Hep showed only Pt−Ni/rGO nanozymes (Figures 2d, S22 and S23). Concentration-dependent fluorescence and UV−vis responses were also observed for the Pt−Ni/rGO−PP2 system (Figures S24 and S25). Notably, in the Pt−Ni/rGO−PP2 system, the fluorescence intensity slightly decreased at low Hep concentrations and then gradually increased with further increasing Hep concentration (Figure S24). This behavior may arise from concentration-dependent PP2−Hep assembly, in which low Hep concentrations promote the binding of multiple PP2 molecules to one Hep chain and induce aggregation-caused quenching, whereas higher Hep concentrations weaken this effect and gradually increase fluorescence.

We further examined the responses of Pt−Ni/rGO−PP4 toward representative GAGs, including hyaluronic acid (HA), Hep, dextran sulfate (DSS), and chondroitin sulfate (Chs) (Figure S26). After incubation with each GAG (100 μg/mL) for 20 min, Pt−Ni/rGO−PP4 showed distinct degrees of fluorescence response (Figure 2e). These differentiated responses arise from variations in anionic group content, charge density, and polysaccharide structure, which affect the binding affinity of each GAG toward cationic porphyrins and its ability to perturb the Pt−Ni/rGO−porphyrin assembly. Because PP2 and PP4 differ in charge density and molecular structure, the same GAG also produced different fluorescence responses in the two porphyrin-based systems (Figures 2e and S27), providing two independent fluorescence outputs. The UV−vis response of the Pt−Ni/rGO−PP4−TMB system toward different GAGs was also evaluated (Figures 2f and S28). Except for HA, the other GAGs induced varying degrees of blue shift of the TMBox absorption peak at 370 nm, likely due to distinct TMBox−GAG assembly behaviors governed by charge density, sulfation degree, and chain structure. SEM observations further confirmed GAG-dependent TMBox assembly. Besides the fibrous Hep−TMBox assemblies, HA induced rod-like assemblies, whereas DSS and Chs generated worm-like aggregates (Figure S29), consistent with their differentiated UV−vis absorption responses. By recording the absorbance at 370 nm, the two Pt−Ni/rGO−porphyrin−TMB systems thus provided two additional colorimetric outputs (Figures 2f, S28 and S30). Together, the fluorescence response signals and UV−vis absorption changes generated four cross-reactive readouts, establishing the basis for dual-channel sensor array-based GAG pattern recognition. Notably, although both channels involve electrostatic interactions, their response trends are not simply correlated, suggesting that the fluorescence and colorimetric outputs provide complementary information for GAG pattern recognition.

In addition, anionic TCPP and neutral TMBP were evaluated as controls (Figure S31). Although Pt−Ni/rGO quenched these porphyrins to different extents, the corresponding Pt−Ni/rGO−TCPP and Pt−Ni/rGO−TMBP systems showed poorly distinguishable fluorescence responses toward GAGs, likely because of their lack of favorable cationic sites for interacting with anionic GAGs. These results further support the use of PP2 and PP4 as fluorescence-responsive components for array construction.

Construction of Dual-Channel Sensor Array for GAG Discrimination

Based on this mechanism, a dual-channel sensor array was constructed by assembling two cationic porphyrins, PP2 and PP4, with negatively charged Pt−Ni/rGO, which quenched the porphyrin fluorescence to different extents. After addition of GAGs, the fluorescence intensity at 670 nm was first recorded under 423 nm excitation. TMB was then added to the same system at a final concentration of 200 μM, followed by incubation at room temperature for 10 min, and the absorbance at 370 nm was measured (Scheme 1). Accordingly, a dual-channel response matrix of four GAGs × 4 channels × 5 replicates was obtained, with the four outputs consisting of two fluorescence responses from the PP2 and PP4 systems and two UV−vis responses from the corresponding TMBox assemblies (Scheme 1). Using the responses to GAGs at 100 μg/mL as a representative example, the four channels exhibited distinct response amplitudes and trends for the four GAGs, indicating good cross-reactivity of the array (Figure 3a,b). After normalization, the response patterns were visualized using a hierarchically clustered heatmap, in which the characteristic fingerprints of different GAGs could be directly observed (Figure 3c).

Hierarchical cluster analysis (HCA) was further performed to assess the similarity among the response patterns. As shown in Figure 3d, the four GAGs formed separate clusters based on Euclidean distances, confirming that the four-dimensional response array could effectively discriminate these polysaccharides. HA was clearly separated from the other GAGs, mainly because its repeating disaccharide unit lacks *O*-sulfate groups and its negative charge primarily arises from carboxyl groups, resulting in a much lower charge density than Hep, DSS, and Chs (Figure S26). Accordingly, HA exhibited weaker interactions with both cationic porphyrins and TMBox, resulting in the smallest fluorescence response and only minor UV−vis spectral changes. In contrast, sulfate-rich Hep, DSS, and Chs generated stronger interactions and more pronounced fluorescence and absorption responses. Further inspection of the HCA dendrogram showed that Hep formed a separate subgroup, whereas DSS and Chs clustered together (Figure 3d). This separation likely arises from differences in their repeating units and functional groups. Hep contains a carboxylate-bearing uronic acid unit compared with DSS but lacks the amide-containing *N*-acetyl group present in Chs (Figure S26). These structural differences may modulate their interactions with cationic porphyrins and TMBox. Overall, the Pt−Ni/rGO-based four-dimensional array effectively captures charge- and structure-dependent differences among GAGs, enabling pattern-based discrimination.

To further evaluate the feasibility and reliability of the dual-channel array, the data matrix of four GAGs × 4 channels × 5 replicates was used as the training set for linear discriminant analysis (LDA). As shown in Figure 3e, the training samples were clearly classified into four groups with 100% accuracy. Three canonical factors were extracted from linear combinations of the response variables, accounting for 64.36%, 30.34%, and 5.30% of the total variance, respectively. To assess the advantage of dual-channel readout, LDA was also performed using only the two fluorescence responses. In this case, the four

https://doi.org/10.1021/acs.analchem.6c03852
Anal. Chem. XXXX, XXX, XXX−XXX

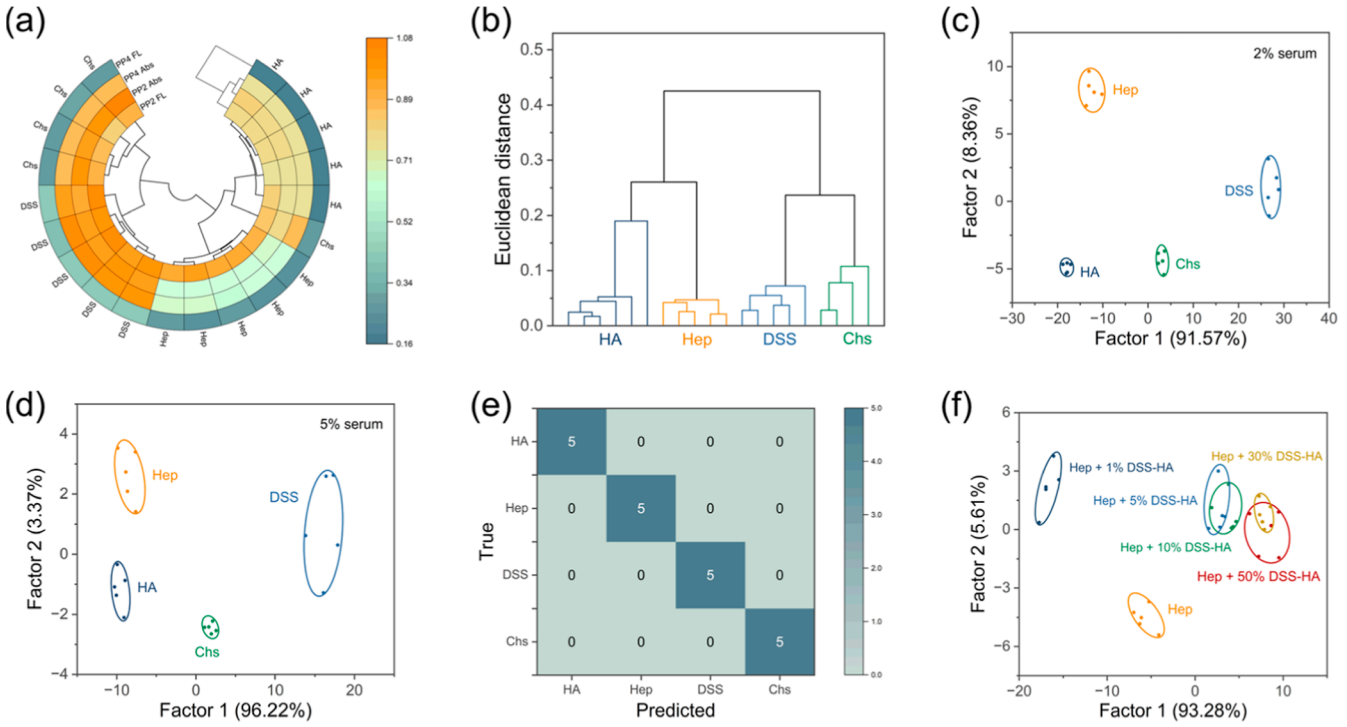

Figure 4. (a) Hierarchical clustering heatmap of normalized response signals of Pt−Ni/rGO−porphyrin sensor array toward GAGs (100 μg/mL) in 2% serum. (b) HCA dendrogram for discrimination of GAGs (100 μg/mL) in 2% serum. LDA canonical score plot for the first two factors obtained from fluorescence and colorimetric responses of sensor array toward GAGs (100 μg/mL) in (c) 2% serum and (d) 5% serum. (e) Confusion matrix plot of the LDA classifier for blind test in 2% serum. (f) LDA canonical score plot of sensor array for discrimination of Hep and Hep samples contaminated with DSS/HA (1:1) at a total concentration of 200 μg/mL.

clusters became closer and less separated (Figure 3f), indicating reduced pattern separability. In contrast, the combined fluorescence and colorimetric responses from a single Pt−Ni/rGO−porphyrin sensor still enabled effective discrimination of the four GAGs (Figures 3g and S32), confirming that one nanozyme-based sensing element can generate information-rich dual-channel outputs.

Beyond the representative concentration of 100 μg/mL, the array also accurately discriminated GAGs at 25, 50, 200, 300, and 500 μg/mL (Figures S33−S37), demonstrating a broad applicable concentration range. The predictive performance of the trained LDA model was further evaluated using blind tests, and the corresponding confusion matrix was shown in Figure 3h. The cross-validation accuracy reached 100%, confirming that the nanozyme sensor array is highly sensitive to subtle structural differences among GAGs, including sulfation degree, uronic acid type, and carboxyl-group distribution. Considering the clinical importance of precise Hep dosage control, the array was further applied to discriminate Hep at different concentrations. As shown in Figures 3i and S38, Hep samples over 0−1 mg/mL were effectively separated, validating the high selectivity and concentration-resolving capability of the proposed dual-channel sensor array. Considering that GAG molecular weight may affect multivalent interactions with the sensing elements and that low-molecular-weight heparin (Low-MW Hep) is also clinically used, we further evaluated five GAG samples, including unfractionated HA, Hep, Low-MW Hep, DSS, and Chs. Their clear separation in the LDA plot indicates that the array can capture molecular-weight-dependent response differences, further supporting its robustness (Figure S39).

Practical Applications of the Dual-Channel Sensor Array

To evaluate the potential of the dual-channel sensor array for Hep recognition in complex biological matrices, we first examined its discrimination capability against several common interferents, including bovine serum albumin (BSA), ATP, Na_3PO_4, and $Na_4P_2O_7$. These species were selected because albumin is the most abundant plasma protein and may cause nonspecific adsorption or signal drift; the level of ATP can increase during platelet activation, cell damage, or inflammatory responses; and phosphate or pyrophosphate species are commonly present in buffer and biological systems. Discrimination assays were performed at 50 and 100 μg/mL and further repeated in the presence of 2% serum to assess matrix tolerance. As shown in Figures S40 and S41, Hep was clearly separated from the interferents at both concentrations in the absence of serum, giving well-resolved clusters in two-dimensional LDA score plots. After introduction of 2% serum, Hep remained distinguishable from the other species (Figures S42 and S43), indicating that the array retained good specificity with minimal interference from serum components.

Given the diverse biological functions and biomedical relevance of GAGs, we further evaluated the applicability of the array in biological matrices by discriminating GAGs in PBS containing 2% or 5% serum at GAG concentrations of 50 or 100 μg/mL. As a representative case, response patterns toward four GAGs at 100 μg/mL in 2% serum were collected and analyzed (Figure S44). After normalization, the data were visualized as a hierarchically clustered heatmap, which displayed distinct response fingerprints for each GAG (Figure 4a). HCA further showed that the four GAGs occupied separate clusters according to Euclidean distances, demonstrating that the four-dimensional response array could discriminate

https://doi.org/10.1021/acs.analchem.6c03852
Anal. Chem. XXXX, XXX, XXX−XXX

GAGs in serum-containing media (Figure 4b). Consistently, LDA of the same data matrix yielded four well-separated clusters (Figure 4c). Reliable discrimination was also achieved under other conditions, including 50 μg/mL GAGs in 2% serum and 100 μg/mL GAGs in 5% serum (Figures 4d, S45 and S46). Although the four GAGs remained distinguishable by LDA in 10% serum, their response clusters were much closer than those obtained in 2% and 5% serum, indicating reduced pattern separability and suggesting that 10% serum is near the practical upper limit of the current two-element array (Figure S47). Cross-validation gave 100% classification accuracy (Figure 4e), further supporting the stability and anti-interference capability of the array in complex matrices.

Finally, the potential of the array for Hep quality control was assessed by distinguishing pure Hep from DSS-contaminated Hep samples. Hep samples containing 1%, 10%, 30%, and 50% (w/w) DSS were analyzed at total GAG concentrations of 100 and 200 μg/mL (Figures S48 and S49). The array clearly differentiated DSS-contaminated Hep from pure Hep, even at a contamination level as low as 1%. Moreover, when Hep was contaminated with a DSS/HA mixture (total concentration, 200 μg/mL; DSS/HA = 1:1), the array still achieved clear discrimination (Figures 4f and S50). These results demonstrated the practical utility of the dual-channel nanozyme sensor array for rapid screening of trace GAG contaminants in Hep and for quality control in complex samples.

CONCLUSIONS

In summary, we developed a dual-channel cross-reactive sensor array for accurate discrimination of Hep and structurally related GAGs. A multifunctional Pt−Ni/rGO nanozyme integrating fluorescence-quenching capability and oxidase-like activity was synthesized. By assembling two cationic NIR porphyrins, PP2 and PP4, with Pt−Ni/rGO, the resulting nanozyme−porphyrin composites generated four cross-reactive outputs through fluorescence responses and TMBox-mediated UV−vis changes. Benefiting from the distinct charge densities and structural features of different GAGs, the machine learning-assisted array enabled reliable pattern recognition of HA, Hep, DSS, and Chs with 100% cross-validation accuracy over a broad concentration range. The platform also detected trace DSS contamination in Hep at levels as low as 1% (w/w). In addition, discrimination assays in serum-containing media and in the presence of common biological interferents demonstrated good matrix tolerance, anti-interference capability, and practical applicability. Although the PP2- and PP4-based colorimetric channels are partially correlated, which may limit further gains in pattern separability, future studies could introduce different chromogenic substrates to generate more diverse colorimetric outputs and enhance discrimination performance. Overall, this work provides a simple and effective strategy for constructing multifunctional nanozyme-based sensor arrays and expands the utility of multichannel pattern-recognition platforms for GAG analysis and Hep quality control.

ASSOCIATED CONTENT

Supporting Information

The Supporting Information is available free of charge at https://pubs.acs.org/doi/10.1021/acs.analchem.6c03852.

TEM images and XPS survey scans of Pt−Ni/rGO; ^{1}H NMR and HRMS of PP2 and PP4; Fluorescence titration profiles of PP2 and PP4 upon addition of Pt−Ni/rGO; Double reciprocal plots of the velocity versus varying concentrations of TMB for Pt−Ni/rGO; Fluorescence response of Pt−Ni/rGO−porphyrin nanocomposite toward various GAGs; UV−vis absorption spectra of Pt−Ni/rGO−porphyrin−TMB system in the presence of various GAGs; Dual-channel sensor array toward GAGs, Hep at different concentrations, Hep and common biologically abundant anions and biomolecules, GAGs in 2% and 5% serum, and Hep samples contaminated with DSS; Comparison of kinetic parameters of Pt−Ni and Pt−Ni/rGO (DOCX)

AUTHOR INFORMATION

Corresponding Authors

Yubin Ding − *Department of Chemistry, College of Sciences, Nanjing Agricultural University, Nanjing, Jiangsu 210095, China;* orcid.org/0000-0002-2208-6509; Email: ybding@njau.edu.cn

Hui Wei − *College of Engineering and Applied Sciences, Nanjing National Laboratory of Microstructures, Jiangsu Key Laboratory of Artificial Functional Materials, Nanjing University, Nanjing, Jiangsu 210023, China; State Key Laboratory of Analytical Chemistry for Life Science, School of Chemistry and Chemical Engineering, Chemistry and Biomedicine Innovation Center (ChemBIC), ChemBioMed Interdisciplinary Research Center at Nanjing University, Nanjing University, Nanjing, Jiangsu 210023, China;* orcid.org/0000-0003-0870-7142; Email: weihui@nju.edu.cn

Xiaoyu Wang − *Department of Chemistry and Material Science, College of Science, Nanjing Forestry University, Nanjing, Jiangsu 210037, China; College of Engineering and Applied Sciences, Nanjing National Laboratory of Microstructures, Jiangsu Key Laboratory of Artificial Functional Materials, Nanjing University, Nanjing, Jiangsu 210023, China;* orcid.org/0000-0002-8641-2430; Email: wangxiaoyu@njfu.edu.cn

Authors

Sijie Li − *Department of Chemistry and Material Science, College of Science, Nanjing Forestry University, Nanjing, Jiangsu 210037, China*

Qing Cheng − *Department of Chemistry and Material Science, College of Science, Nanjing Forestry University, Nanjing, Jiangsu 210037, China*

Qi Sun − *College of Engineering and Applied Sciences, Nanjing National Laboratory of Microstructures, Jiangsu Key Laboratory of Artificial Functional Materials, Nanjing University, Nanjing, Jiangsu 210023, China;* orcid.org/0009-0004-3613-2774

Chunfei Bao − *Department of Chemistry, College of Sciences, Nanjing Agricultural University, Nanjing, Jiangsu 210095, China*

Guangyu Bu − *Department of Chemistry and Material Science, College of Science, Nanjing Forestry University, Nanjing, Jiangsu 210037, China*

Shuaishuai Zhu − *School of Materials Science and Engineering, Nanjing Institute of Technology, Nanjing, Jiangsu 211167, China*

Complete contact information is available at: https://pubs.acs.org/10.1021/acs.analchem.6c03852

Author Contributions

#S.L. and Q.C. contributed equally. All authors have given approval to the final version of the manuscript.

Notes

The authors declare no competing financial interest.

■ ACKNOWLEDGMENTS

This work was supported by the Natural Science Foundation of Jiangsu Province (BK20241895), the National Natural Science Foundation of China (22104055, 22374071, and 22278229), the State Key Laboratory of Analytical Chemistry for Life Science (5431ZZXM2501), the Fundamental Research Funds for the Central Universities (2026300425), the PAPD Program, the Key Program of Nanozyme Laboratory in Zhongyuan (NLZ-KP2024NIC06), Jiangsu Provincial Key R&D Program (BE2022836), and the International Expansion and Enhancement Program by Nanjing University International Affairs Office.

■ REFERENCES

(1) Kuschert, G. S.; Coulin, F.; Power, C. A.; Proudfoot, A. E.; Hubbard, R. E.; Hoogewerf, A. J.; Wells, T. N. Glycosaminoglycans interact selectively with chemokines and modulate receptor binding and cellular responses. *Biochemistry* **1999**, *38* (39), 12959−12968.

(2) Bayat, P.; Rambaud, C.; Priem, B.; Bourderioux, M.; Bilong, M.; Poyer, S.; Pastoriza-Gallego, M.; Oukhaled, A.; Mathé, J.; Daniel, R. Comprehensive structural assignment of glycosaminoglycan oligo- and polysaccharides by protein nanopore. *Nat. Commun.* **2022**, *13*, 5113.

(3) Ricard-Blum, S.; Perez, S. Glycosaminoglycan interaction networks and databases. *Curr. Opin. Struct. Biol.* **2022**, *74*, 102355.

(4) Lever, R.; Page, C. R. Novel drug development opportunities for heparin. *Nat. Rev. Drug Discovery* **2002**, *1*, 140−148.

(5) Uebelhart, D. Clinical review of chondroitin sulfate in osteoarthritis. *Osteoarthr. Cartil.* **2008**, *16*, S19−S21.

(6) Guerrini, M.; et al. Oversulfated chondroitin sulfate is a contaminant in heparin associated with adverse clinical events. *Nat. Biotechnol.* **2008**, *26*, 669−675.

(7) Noguchi, T.; Roy, B.; Yoshihara, D.; Sakamoto, J.; Yamamoto, T.; Shinkai, S. Emergent Molecular Recognition through Self-Assembly: Unexpected Selectivity for Hyaluronic Acid among Glycosaminoglycans. *Angew. Chem., Int. Ed.* **2016**, *55* (19), 5708−5712.

(8) Szajek, A. Y.; Chess, E.; Johansen, K.; Gratzl, G.; Gray, E.; Keire, D.; Linhardt, R. J.; Liu, J.; Morris, T.; Mulloy, B.; Nasr, M.; Shriver, Z.; Torralba, P.; Viskov, C.; Williams, R.; Woodcock, J.; Workman, W.; Al-Hakim, A. The US regulatory and pharmacopeia response to the global heparin contamination crisis. *Nat. Biotechnol.* **2016**, *34* (6), 625−630.

(9) Li, G. Y.; Cai, C.; Li, L. Y.; Fu, L.; Chang, Y. Q.; Zhang, F. M.; Toida, T.; Xue, C. H.; Linhardt, R. J. Method to Detect Contaminants in Heparin Using Radical Depolymerization and Liquid Chromatography-Mass Spectrometry. *Anal. Chem.* **2014**, *86* (1), 326−330.

(10) Yan, N.; Song, F. F.; Ouyang, Y. L.; Li, D. X.; Tian, H.; Yi, L.; Linhardt, R. J.; Zhang, Z. Q. Glycan Mapping of Low-Molecular-Weight Heparin Using Mass Spectral Correction Based on Chromatography Fitting with "Glycomapping" Software. *Anal. Chem.* **2022**, *94* (38), 13000−13009.

(11) Kim, D.; Lee, U.; Bouffard, J.; Kim, Y. Glycosaminoglycan-Induced Emissive J-Aggregate Formation in a meso-Ester BODIPY Dye. *Adv. Opt. Mater.* **2020**, *8* (14), 1902161.

(12) Subedi, S.; Hwang, H. J.; Kang, D. H.; Mehta, P. K.; Kim, N.; Park, H.; Lee, J. S.; Lee, K. H. Development of peptide-based ratiometric fluorescent probe for sensing heparan sulfate and heparin in aqueous solutions at physiological pH and quantitative detection of heparan sulfate in live cells. *Biosens. Bioelectron.* **2023**, *238*, 115595.

(13) Yang, Z. Y.; Fan, L. F.; Fan, X.; Hou, M. T.; Cao, Z. Y.; Ding, Y. B.; Zhang, W. H. Porphyrin-GO Nanocomposites Based NIR Fluorescent Sensor Array for Heparin Sensing and Quality Control. *Anal. Chem.* **2020**, *92* (9), 6727−6733.

(14) Ding, Y. B.; Wang, J. X.; Wang, R. A.; Xie, Y. S. Development of porphyrin-based fluorescent sensors and sensor arrays for saccharide recognition. *Chin. Chem. Lett.* **2024**, *35* (2), 109008.

(15) Dalton, C. E.; Quinn, S. D.; Rafferty, A.; Morten, M. J.; Gardiner, J. M.; Magennis, S. W. Single-Molecule Fluorescence Detection of a Synthetic Heparan Sulfate Disaccharide. *ChemPhysChem* **2016**, *17* (21), 3442−3446.

(16) Cui, J.; Zang, S. P.; Shu, W.; Nie, H. L.; Jing, J.; Zhang, X. L. Highly Sensitive and Selective Detection of Heparin in Serum Based on a Long-Wavelength Tetraphenylethylene-Cyanopyridine Aggregation-Induced Emission Luminogen. *Anal. Chem.* **2020**, *92* (10), 7106−7113.

(17) Wang, J. X.; Fan, Y. S.; Tian, Y. F.; Ge, X. N.; Zhang, W. H.; Ding, Y. B. A π-Extended AIE Platform for Pattern Recognition of Glycosaminoglycans. *Anal. Chem.* **2025**, *97* (5), 3045−3052.

(18) Geng, Y.; Peveler, W. J.; Rotello, V. M. Array-based "Chemical Nose" Sensing in Diagnostics and Drug Discovery. *Angew. Chem., Int. Ed.* **2019**, *58* (16), 5190−5200.

(19) Li, T.; Zhu, X. Y.; Hai, X.; Bi, S.; Zhang, X. J. Recent Progress in Sensor Arrays: From Construction Principles of Sensing Elements to Applications. *ACS Sens.* **2023**, *8* (3), 994−1016.

(20) Yu, Y.; Ni, W. W.; Shi, X.; Bian, Y.; Li, H. H.; Liu, M.; Chen, W. J.; Zhang, M.; Jiang, S. J.; Cheng, M. Q.; Li, F.; Zhang, Y. L.; Zhang, Z. J.; Huang, H.; Han, J. S. A Supramolecular Fluorescent Sensor Array Composed of Conjugated Fluorophores and Cucurbit 7 uril for Bacterial Recognition. *Anal. Chem.* **2024**, *96* (36), 14490−14498.

(21) Zhang, W. X.; Song, Y. X.; Lv, Y. J.; Sun, J.; Cui, Y. H.; Li, X.; Ma, M. W.; Wang, X.; Su, Z. M. Smartphone-Integrated Fluorescent Sensing Array Assembled from Lanthanide Metal-Organic Frameworks for Rapid Identification and Differentiation of Antibiotics in Daily Foods. *Anal. Chem.* **2025**, *97* (34), 18742−18749.

(22) Chi, J.; Qin, Y. X.; Song, Y. Y.; Feng, L. Single-Component Dual-Emissive MOF Sensor Array for Fingerprint Identification of Multiplex Antibiotics. *Anal. Chem.* **2025**, *97* (33), 18299−18307.

(23) Gao, L.; Zhuang, J.; Nie, L.; Zhang, J.; Zhang, Y.; Gu, N.; Wang, T.; Feng, J.; Yang, D.; Perrett, S.; Yan, X. Intrinsic peroxidase-like activity of ferromagnetic nanoparticles. *Nat. Nanotechnol.* **2007**, *2*, 577−583.

(24) Huang, Y.; Ren, J.; Qu, X. Nanozymes: classification, catalytic mechanisms, activity regulation, and applications. *Chem. Rev.* **2019**, *119* (6), 4357−4412.

(25) Zandieh, M.; Liu, J. W. Nanozymes: Definition, Activity, and Mechanisms. *Adv. Mater.* **2024**, *36* (10), 2211041.

(26) Zhang, Y.; Wei, G.; Liu, W.; Li, T.; Wang, Y.; Zhou, M.; Liu, Y.; Wang, X.; Wei, H. Nanozymes for nanohealthcare. *Nat. Rev. Methods Primers* **2024**, *4*, 36.

(27) Zhang, R.; Jiang, B.; Fan, K.; Gao, L.; Yan, X. Designing nanozymes for in vivo applications. *Nat. Rev. Bioeng.* **2024**, *2*, 849−868.

(28) Shamsabadi, A.; Haghighi, T.; Carvalho, S.; Frenette, L. C.; Stevens, M. M. The Nanozyme Revolution: Enhancing the Performance of Medical Biosensing Platforms. *Adv. Mater.* **2024**, *36* (10), 2300184.

(29) Shao, S. K.; Hirschbiegel, C. M.; Allan, E. F.; Somerville, S. V.; Gooding, J. J.; Rotello, V. M.; Xia, X. H. Can nanozymes achieve more than enzymes? *Nat. Rev. Mater.* **2026**, *11* (5), 413−429.

(30) Wang, X. Y.; Qin, L.; Zhou, M.; Lou, Z. P.; Wei, H. Nanozyme Sensor Arrays for Detecting Versatile Analytes from Small Molecules to Proteins and Cells. *Anal. Chem.* **2018**, *90* (19), 11696−11702.

(31) Xia, J. N.; Li, Z.; Ding, Y. P.; Shah, L. A.; Zhao, H. B.; Ye, D. X.; Zhang, J. J. Construction and Application of Nanozyme Sensor Arrays. *Anal. Chem.* **2024**, *96* (21), 8221−8233.

(32) Shi, Q. H.; Li, Z. Y.; Wang, Y.; Liu, F. F.; Jing, W. J. Machine Learning-Enhanced Nanozyme Sensor Array for Accurate Multiple

Quinolone Antibiotics Recognition. *Anal. Chem.* **2025**, *97* (32), 17552−17561.
(33) Zhao, Q. L.; Luan, T.; Sun, J.; Huang, J. S.; Du, Y.; Yang, X. R. Cu-Based Nanozyme-Enabled Triple Channel Colorimetric Sensor Arrays for Efficient Discrimination of Flavonoids. *Anal. Chem.* **2025**, *97* (35), 19038−19046.
(34) Li, X.; Wu, S. Q.; Ding, S. C.; Wang, Z.; He, J.; Sun, M. X.; Al-Mashriqi, H. S.; Tang, S.; Chen, J.; Qiu, H. D. Machine Learning-Assisted Fe-N-C Single-Atom Nanozyme Rapid Screening Platform for Acetylcholinesterase Inhibitors. *Anal. Chem.* **2025**, *97* (46), 25840−25852.
(35) Shen, X. Y.; Ma, S. R.; Song, C. C.; He, Y. Z.; Li, M. G. Kinetic and Mechanistic Discrepancies of Single/Dual-Atom Nanozymes Drive a Triple-Channel Sensing Array for Machine Learning-Assisted Antioxidant Discrimination. *Anal. Chem.* **2025**, *97* (36), 19957−19970.
(36) Wei, D. L.; Li, M. F.; Yang, Y. D.; Deng, C. M.; Zhu, F.; Li, M.; Deng, Y. B.; Zhang, Z. Ligand Microenvironment-Regulated Nanozymes Enabled Machine Learning-Assisted Sensor Array for Simultaneous Identification of Phenolic Pollutants. *ACS Sens.* **2025**, *10* (7), 5245−5255.
(37) Wu, Q.; Sun, F.; Kong, H. X.; Liu, B.; Jiang, Z. W.; Zhang, P.; Wang, Y. NIR-Responsive AuAgPt Plasmonic Nanozyme: Colorimetric/Photothermal Dual-Signal Sensing Array for Discriminating and Detecting Sulfur-Containing Compounds. *Anal. Chem.* **2026**, *98* (12), 9027−9037.
(38) Ma, X. X.; Zhu, X. Y.; Zhu, Z. J.; Ma, Q.; Jia, S. C.; Wu, N.; Zhou, X. Y.; Hai, X.; Bi, S. A Biomimetic Nanozyme Engineered via Coordination and Confinement for Photothermal-Reinforced Catalytic Detection of Extracellular Vesicles and Diagnosis of Cancer. *Anal. Chem.* **2026**, *98* (19), 14447−14459.
(39) Gao, Z. Y.; Long, C.; Cheng, Y. J.; Guan, J. P.; Yao, Y.; Tang, W. L.; Chen, S. Y.; Liu, Q.; Chen, X. Q. Substrate-Driven Coenzyme Activating Oxidase-Like Activity of Copper-Based Nanozymes for Robust Profiling of Sulfonamides. *Anal. Chem.* **2026**, *98* (8), 6226−6235.
(40) Wang, X.; Li, Q. Q.; Ma, J. Y.; Zhang, X. P.; Wu, X.; Han, Q.; Jian, Z. Y.; Wang, L. H.; Yan, B.; Wu, H. A.; Ma, M.; Ge, Z.; Zhang, Y. Molecularly Imprinted Nanozyme Intelligent Array Sensing Platform Realizes the Enrichment and Quantitative Detection of Small Extracellular Vesicles. *Anal. Chem.* **2026**, *98* (14), 10444−10456.
(41) Wei, M. M.; Zhang, Q. K.; Huang, H. J.; Shu, Y. Mn Ce-CDs-Loaded MIL-53(Fe) Nanozymes Multisubstrate Sensor Array Integrated with Multiple Machine Learning Complementary Strategy for Highly Reliable Antioxidant Discrimination and Determination. *Anal. Chem.* **2026**, *98* (2), 1541−1554.
(42) Wang, H.; Han, Y. Q.; Tian, S.; Wang, M. K.; Wang, S. Engineering a Metal-Organic Framework-Dominated Bioinspired Multienzymatic Sensor Array for Portable Detection of Perfluoroalkyl Substances. *Anal. Chem.* **2025**, *97* (43), 24115−24125.
(43) Guo, J. Y.; Wang, G.; She, Y. F.; Li, K.; Liu, Y. J.; Sun, Z. Y.; Chen, Z. B. Atomic Engineering of a FeFe Dual Single-Atom Nanozyme for Enhanced Peroxidase-like Activities To Build Chemical Tongue for Discrimination of Aromatic Amines. *Anal. Chem.* **2025**, *97* (36), 19889−19899.
(44) Heidary, O.; Ashrafi, H.; Akhond, M.; Hemmateenejad, B. Array of Manganese-Based Bimetallic Metal-Organic-Framework Nanozymes with Enhanced Oxidase-like Catalytic Activity Can Simultaneously Identify and Measure Antioxidants. *Anal. Chem.* **2025**, *97* (9), 4860−4870.
(45) Yan, B. S.; Liu, W. D.; Chu, S. S.; Li, J. K.; Lu, Y. Z.; Liu, Z. M. Multidimensional Engineering of Single-Atom Iron Nanozymes for Machine Learning-Assisted Multiplexed Sensing. *Anal. Chem.* **2026**, *98* (18), 13915−13924.
(46) Liu, B. W.; Sun, Z. Y.; Huang, P. J. J.; Liu, J. W. Hydrogen Peroxide Displacing DNA from Nanoceria: Mechanism and Detection of Glucose in Serum. *J. Am. Chem. Soc.* **2015**, *137* (3), 1290−1295.
(47) Zhang, L.; Tan, Q. G.; Xiao, S. J.; Yang, G. P.; Liu, X.; Zheng, Q. Q.; Fan, J. Q.; Liang, R. P.; Qiu, J. D. DNAzyme-Derived Aptamer Reversely Regulates the Two Types of Enzymatic Activities of Covalent-Organic Frameworks for the Colorimetric Analysis of Uranium. *Anal. Chem.* **2023**, *95* (10), 4703−4711.
(48) Fan, K.; Cao, C.; Pan, Y.; Lu, D.; Yang, D.; Feng, J.; Song, L.; Liang, M.; Yan, X. Magnetoferritin nanoparticles for targeting and visualizing tumour tissues. *Nat. Nanotechnol.* **2012**, *7*, 459−464.
(49) Qi, Q. J.; Guan, P. C.; Zhang, Y. X.; Yu, Y. F.; Zhang, G.; Lin, J. S.; Zhang, Y. J.; Li, J. F. In Situ Synthesis of 3D Au@Pt Nanozyme Hydrogel SERS Substrates for Highly Sensitive and Quantitative Sensing. *ACS Sens.* **2025**, *10* (11), 8694−8701.
(50) Fu, C. C.; Li, Y. L.; Lei, X. Y.; Su, J. C.; Chen, Y. L.; Wu, Y.; Shi, W. B.; Tan, X. P.; Li, Y. Y.; Jung, Y. M. SERS Sensor for Acetylcholine Detection Based on Covalent Organic Framework Hybridized Gold Nanoparticles As Nanozymes. *Anal. Chem.* **2024**, *96* (47), 18585−18589.
(51) Zhao, Q. N.; Hu, S. Z.; Wang, F.; Lin, F.; Zhao, B.; Song, W. SERS-Nanozyme Cooperative Ag@Lacunary-POM Nanoclusters for Exosome Biosensing. *ACS Sens.* **2025**, *10* (11), 8821−8828.
(52) Zhou, X. M.; Huang, S. J.; Guo, W. F.; Liu, W. F.; Wen, M. Y.; Shang, L. Multicolor Gold Clusterzyme-Enabled Construction of Ratiometric Fluorescent Sensor Array for Visual Biosensing. *Anal. Chem.* **2024**, *96* (47), 18873−18879.
(53) Li, X.; Yang, X. Q.; Wu, J.; Yang, Z. J.; Zhu, X. S. A Novel Four-Channel Sensor Array with Dual Enzymes and Dual Modes for Evaluating Total Antioxidant Capacity in Foods. *ACS Sens.* **2025**, *10* (4), 2883−2894.
(54) Zheng, J. J.; Zhu, F. Y.; Song, N. N.; Deng, F.; Chen, Q.; Chen, C.; He, J. Y.; Gao, X. F.; Liang, M. M. Optimizing the standardized assays for determining the catalytic activity and kinetics of peroxidase-like nanozymes. *Nat. Protoc.* **2024**, *19*, 3470−3488.
(55) Wang, X. Y.; Wei, G.; Liu, W. L.; Zhang, Y. H.; Zhu, C. X.; Sun, Q.; Zhang, M. X.; Wei, H. Platinum-Nickel Nanoparticles with Enhanced Oxidase-like Activity for Total Antioxidant Capacity Bioassay. *Anal. Chem.* **2023**, *95* (14), 5937−5945.
(56) Stankovich, S.; Dikin, D. A.; Piner, R. D.; Kohlhaas, K. A.; Kleinhammes, A.; Jia, Y.; Wu, Y.; Nguyen, S. T.; Ruoff, R. S. Synthesis of graphene-based nanosheets via chemical reduction of exfoliated graphite oxide. *Carbon* **2007**, *45* (7), 1558−1565.
(57) Niu, X. H.; Wang, M. Z.; Zhu, H. J.; Liu, P.; Pan, J. M.; Liu, B. X. Nanozyme catalysis-assisted ratiometric multicolor sensing of heparin based on target-specific electrostatic-induced aggregation. *Talanta* **2022**, *238*, 123003.

https://doi.org/10.1021/acs.analchem.6c03852
Anal. Chem. XXXX, XXX, XXX−XXX